ELSEVIER

Journal of Fluids and Structures 25 (2009) 848–866

JOURNAL OF FLUIDS AND STRUCTURES

www.elsevier.com/locate/jfs

Suppressing vortex-induced vibrations via passive means

H. Baek, G.E. Karniadakis*

Division of Applied Mathematics, Brown University, Providence, RI 02912, USA

Received 4 August 2008; accepted 1 March 2009
Available online 1 May 2009

Abstract

We investigate numerically the hydrodynamic effect of a slit in circular cylinders with the goal of finding a geometric modification that minimizes vortex-induced vibrations (VIV) without any energy consumption. A slit parallel to the incoming flow is found to be very effective in suppressing VIV by either weakening or detuning vortex shedding. Through a series of simulations, the optimal size of the slit to suppress VIV is found at Reynolds number 500; this size is smaller at a higher $Re = 1000$. The effectiveness of the slit in suppressing VIV is confirmed over a wide range of values of the reduced velocity. Modified cylinders with a slit of sufficiently large width cause a strong jet flow into the wake that changes the vortex shedding pattern dramatically. For slits larger than the critical width, the instantaneous flow fields do not show periodic vortex shedding. While unsteadiness of the flow persists in these cases, it is the effective *detuning* process of the jet flow interacting with the wake flow that leads to VIV suppression. A linear stability analysis shows that jet flow through a slit changes the stability in the wake of cylinder by inducing two small pockets of absolute instability at the back of the cylinder followed by bands of convectively and absolutely unstable regions. We also present results with alternative geometry modifications using perforated thin shells.

Keywords: VIV; Passive control; CFD; Stability analysis; Wake flow

1. Introduction

A recent simulation study of Dong et al. (2008) shows that windward suction combined with leeward blowing around a circular cylinder can eliminate vortex shedding and consequently suppress vortex-induced vibrations (VIV). The stability analysis of the wake presented in that paper indicates that this suppression is due to the change in the instability mode from absolute to convective. This effective method, however, is costly from the implementation standpoint as it requires energy expenditure to maintain the necessary suction and/or blowing. Our present study aims to find a simplified way to implement the suction/blowing idea in a passive manner, i.e., without any energy consumption.

We performed numerous simulations of a cylinder with a slit placed at various angles and not necessarily along the diameter, and a cylinder covered with a thin shell which is dented at various locations with different dent sizes. As we expected from the study of Dong et al. (2008), a cylinder with a streamwise-oriented (“parallel”) slit was found to be the most effective in reducing the drag and lift forces; a shrouded cylinder was also effective but less so. When vertical or

*Corresponding author. Tel.: +1 401 863 1217; fax: +1 401 863 2722.
E-mail address: gk@dam.brown.edu (G.E. Karniadakis).

0889-9746/$ - see front matter © 2009 Elsevier Ltd. All rights reserved.
doi:10.1016/j.jfluidstructs.2009.02.006

slanted slits are placed along the diameter, in the frontal section, or near the base of the cylinder, they show unfavorable effects on VIV, namely stronger vortex shedding and higher shedding frequency as observed in the experiments of Igarashi (1978) and Olsen and Rajagopalan (2000). Hence, configurations other than a parallel slit were not further pursued but some results including the drag and lift forces on the fixed cylinder covered with shells are presented here as a practical way of implementing the concept of VIV suppression with slit.

Even though many techniques to suppress VIV have been proposed in the literature, a thorough study of a vibrating cylinder with a slit has not been performed yet, to the best knowledge of the authors. Igarashi (1978) studied experimentally the effect of a slit in a *stationary* cylinder on the wake flow in the Reynolds number range of $\mathcal{O}(10^5)$, changing the angle of the slit to the incoming flow from $0^\circ$to 90°. He observed that a slit of angle less than 40° moves the vortex formation region downstream and increases the base pressure. A slit with an angle larger than 60° increases the wake width which decreases the base pressure and the shedding frequency due to strong separated vortices. Boundary layer suction (blowing) was observed on the upper (lower) side of the cylinder when a vortex forms on the upper (lower) side after a vortex is already shed on the lower (upper) side. This suction was reported to delay the separation of the boundary layer causing the formation of strong separated vortices. Also, Olsen and Rajagopalan (2000) reported an experimental study on the vortex shedding and drag coefficient of modified circular cylinders, namely circular cylinders with a slit and/or a concave rear notch. They observed higher drag coefficient and strong and stable vortex shedding pattern at $\mathrm{Re} = 2200$ for the case of a cylinder with a slit normal to the flow.

Wake flows past a pair of circular cylinders side-by-side have similarity with our configuration when the gap between the two cylinders is small; see Sumner et al. (1999), Williamson (1985), Bearman (1973) and Lee et al. (2009). Since a cylinder with a slit directs the incoming flow into the wake in a passive way, the method is similar to Wong's self-sustained fluid injection and Grimminger's guide vane cited in Naudascher and Rockwell (1994). Also, relevant are the studies on the flow structure change and control via suction/blowing on a bluff body reported by many researchers including Wood (1964), Lin et al. (1995) and Kim and Choi (2005). VIV control via a slit, however, has not been studied systematically. Hence, we carried out numerical simulations at $\mathrm{Re} = 500$ and 1000 with stationary cylinders but also cylinders free to vibrate in the crossflow (Y) direction as well as in both the streamwise (X) and crossflow (Y) directions. To gain some insight into the flow modification the slit causes, we employed local linear stability analysis to understand the change of global stability of the wake. Triantafyllou et al. (1986) and Karniadakis and Triantafyllou (1989) showed the dominant frequency of the wake can be accurately predicted through this stability analysis for uncontrolled wakes. In the present study, the linear stability analysis is useful in quantifying the changes of the wake for different cases.

In this paper, we first present a brief account of numerical method and configuration in Section 2. The results of simulations with fixed cylinders and VIV simulations with crossflow-free and totally free cylinders appear in Sections 3.1, 3.2 and 3.3, respectively. Findings from the temporally averaged flow and corresponding local linear stability analysis are discussed in Section 4. Some results with shelled cylinders—potential practical implementations of slit flows—are presented in Section 5, followed by conclusions in Section 6.

2. Configuration and numerical method

A slit is placed parallel to the incoming flow along the diameter of a circular cylinder as shown in Fig. 1. The width of the slit varied from 0% to 30% of the diameter of the cylinder. The same configurations were used for the stationary cylinders as well as for the VIV simulations. A typical 2-D computational domain for $\mathrm{Re} = 500$ is shown in Fig. 1 with $-10 \leqslant x \leqslant 50$ and $-10 \leqslant y \leqslant 10$. The origin of the coordinate system is located at the center of the cylinder and the positive x-axis is pointing downstream.

For stationary cylinders and shelled cylinders, we solve the incompressible Navier–Stokes equations

$$\frac{\partial u}{\partial t} + (u \cdot \nabla)u = -\nabla p + \frac{1}{\mathrm{Re}}\nabla^2 u, \tag{1a}$$

$$\nabla \cdot u = 0, \tag{1b}$$

with no-slip boundary condition on a cylinder; the incoming flow is uniform and steady; the top and bottom sides of the domain are periodic; the outflow is assumed to be fully developed. These equations were solved with NEKTAR, which implements the spectral/hp element method and utilizes the Jacobi polynomial basis to represent the geometry, velocity and pressure; for more details, refer to Karniadakis and Sherwin (2005). This solver employs a high-order splitting scheme and each time step consists of three substeps. At the first substep, it updates the solution treating explicitly the nonlinear convection term. Then, the pressure is obtained by a Poisson equation using an updated intermediate velocity

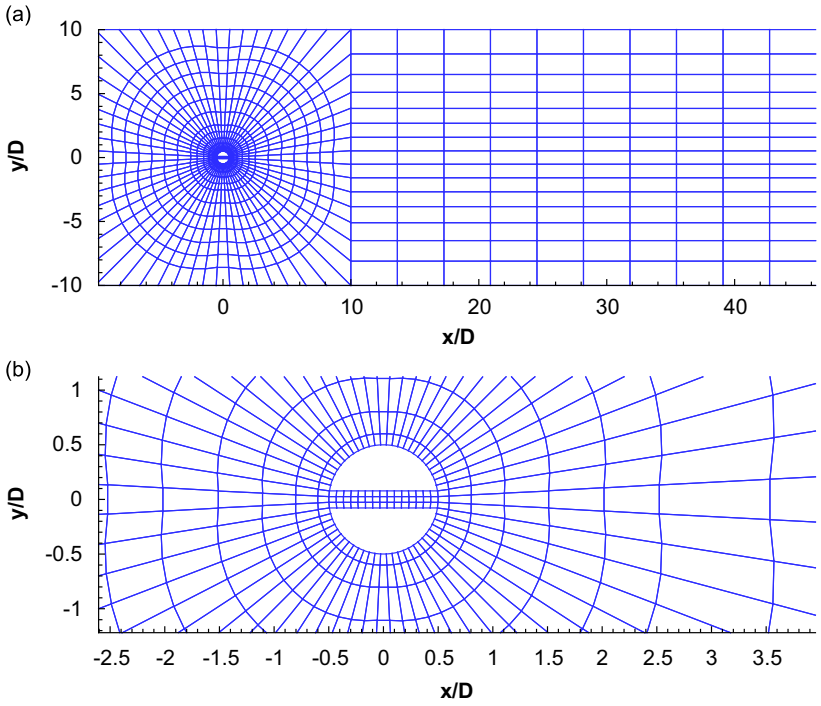

Fig. 1. (a) Computational domain around a cylinder. (b) Quadrilateral elements are used in the slit and around the cylinder. The cylinder diameter is $D = 1$.

and Neumann pressure boundary conditions. At the third substep, the new velocity is obtained by solving three inhomogeneous Helmholtz equations.

For the VIV simulation of free cylinders, the Navier–Stokes equations are written in the body-fixed coordinates for the fluid domain, and the momentum equations include the extra acceleration terms due to the moving reference frame. Boundary conditions are modified to take into account the motion of the coordinates. The cylinder motion, both in X and Y directions, was assumed to be linear without rotation, and described by

$$\ddot{y} + 2\zeta\omega_n\dot{y} + \omega_n^2 y = \frac{f}{m}, \tag{2}$$

where ω_n, ζ, and f are the natural frequency of the system, damping coefficient, and hydrodynamic forces, respectively. The two systems are coupled by transferring the hydrodynamic forces to the structure solver (2) as external forces (pressure and viscous components) with updated cylinder position and velocity. The XY motions are updated through the second-order accurate Newmark integration scheme. The assumption of linear motion of a cylinder and coordinate transformation made the remeshing or interpolation unnecessary even when the cylinder undergoes large displacements. For details, we refer to Newman and Karniadakis (1997).

In order to guarantee that our numerical solutions do not depend on the size of numerical domains, we performed sensitivity tests with larger domains. The domain is discretized densely inside and near the cylinder boundary so that the spectral elements around the cylinder are sufficiently fine to capture the boundary layer. The numbers of elements range from 500 to 1200. For simulations with stationary cylinders at $\mathrm{Re} = 1000$ and moving cylinders at $\mathrm{Re} = 500$, the size of domains and the number of elements were increased proportionally in order to prevent any contaminating errors due to the periodic boundary condition along the Y direction and outflow boundary condition along the X direction. In all cases, the Reynolds number is based on the incoming flow velocity and the cylinder diameter. Most of the simulations were done at $\mathrm{Re} = 500$; selective simulations at $\mathrm{Re} = 1000$ were also carried out.

Simulations were performed mostly in 2-D because 3-D simulations are significantly more expensive than 2-D cases for our parametric study. In general, 2-D simulations of a cylinder are known to overpredict the mean drag and root mean square (r.m.s.) lift coefficients, see Persillon and Braza (1998) and references therein, but they underpredict the VIV amplitude, see Evangelinos and Karniadakis (1999). In this study, a 3-D simulation for one particular case, $s/D = 0.2$, is carried out to confirm the effect of three-dimensionality of the flow on the drag and lift forces. In 3-D flow

simulation, the solution is assumed to be periodic in the spanwise direction with its nondimensional length 3π. The spectral element/Fourier method developed by Karniadakis (1990) is employed. Hence, the same spatial discretization (mesh) on the plane normal to spanwise direction is used, and 64 Fourier modes are employed to describe the solution along the spanwise direction. To expedite the transition from 2-D to 3-D state, spanwise body forces over $0.1-0.2$ convective time units are introduced by adding random amplitude Fourier modes in the lower frequency range; then they are set to zero.

3. Results

3.1. Stationary cylinder

Firstly, we perform 2-D simulations to investigate the effect of a slit in a stationary cylinder in uniform flow at $\mathrm{Re} = 500$ and 1000. Table 1 shows the simulation cases with varying slit ratios, s/D, where s and D are the slit width and the diameter of a cylinder, respectively. Case ST1, $s/D = 0.0$, is the uncontrolled reference case. As expected, the flow through the slit moves the vortex formation downstream and modifies the antisymmetric pattern of the vortex shedding through interactions of slit vortices with those from the cylinder outer wall as shown in Fig. 2. For small slits up to $s/D = 0.16$, vortex shedding pattern is not different from that of the reference case, i.e., a cylinder without a slit. Cases ST6 and ST7, however, show more complicated and irregular vortex shedding and the slit jet is biased towards upper side, lower side, or parallel to the incoming flow. A period of change in direction was not established in contrast to reports by Kim and Durbin (1988) and Sumner et al. (1999). For these cases, the vortex shedding from the slit becomes stronger and more easily noticeable than in case ST5 but it also disappears as in cases with a narrow slit width.

When vortices from the slit are not strong ($s/D < 0.16$), they only contribute to the elongation of the shear layer and they eventually disappear in the near-wake. In case ST5, the region of vortex formation behind the cylinder is pushed downstream farthest while the lift force reaches a minimum. When $s/D > 0.16$, vortices from the slit are shed and interact with the vortices of the same or opposite sign from the cylinder outer wall. Hence, the vortex street becomes very irregular and the time-periodicity of the lift and drag forces disappears. Case ST6 demonstrates that the slit jet induces a symmetric vortex shedding before the flow reaches stationary state, which is characterized by chaotic vortex shedding. Specifically, a competition between the symmetric and anti-symmetric instability modes is observed which leads to intermittent behavior. During the irregular vortex shedding, there are short time periods when the vortex shedding becomes more or less symmetric due to the symmetric instability mode of the slit jet.

The time histories of drag and lift force coefficient are plotted in Fig. 3; we observe the dramatic changes of the lift forces as the slit ratio increases. The periodicity of the vortex shedding of case ST5 still seems to have the dominant single frequency in the lift and drag; the lift force amplitude, however, reduces to less than 10% of that of the reference cylinder. Also, the drag force decreases gradually as s/D increases. For cases with slit ratio larger than 0.16, the drag and force time histories become chaotic due to competition between antisymmetric Karman vortex shedding from the cylinder and the symmetric shedding from the jet.

We also calculated the r.m.s. values of the lift force time history to compare the different cases as shown in Fig. 4. The r.m.s. lift coefficient diminishes up to the slit ratio 0.16 and then increases slightly as the slit ratio increases further, so that the r.m.s. of case ST7 is larger than that of case ST6. The increase of r.m.s. lift coefficient agrees with the amplitude increase in the lift force time history. We confirmed that this optimum slit size becomes smaller when the Reynolds

Table 1
Peaks of the power spectrum of the lift force in a stationary cylinder at $\mathrm{Re} = 500$.

Cases	s/D	f_1	f_2	f_3	f_4
ST1	0.0	0.235(0.943)	0.705(−2.140)	1.174(−4.187)	1.642(−6.164)
ST2	0.05	0.233(0.804)	0.699(−2.374)	1.169(−4.563)	1.630(−6.359)
ST3	0.12	0.210(0.456)	0.627(−3.430)	1.046(−4.802)	1.462(−5.89)
ST4	0.14	0.249(−1.039)	0.745(−4.825)	1.245(−7.235)	1.742(−7.234)
ST5	0.16	0.073(−3.687)	0.265(−2.143)	0.579(−6.123)	0.767(−7.566)
ST6	0.20	0.092(−0.318)	0.279(−1.633)	0.465(−1.935)	0.625(−3.169)
ST7	0.30	0.027(−1.015)	0.069(−1.111)	0.142(−0.857)	0.300(−1.751)

Numbers in parentheses are magnitudes in log scale at the corresponding frequency.

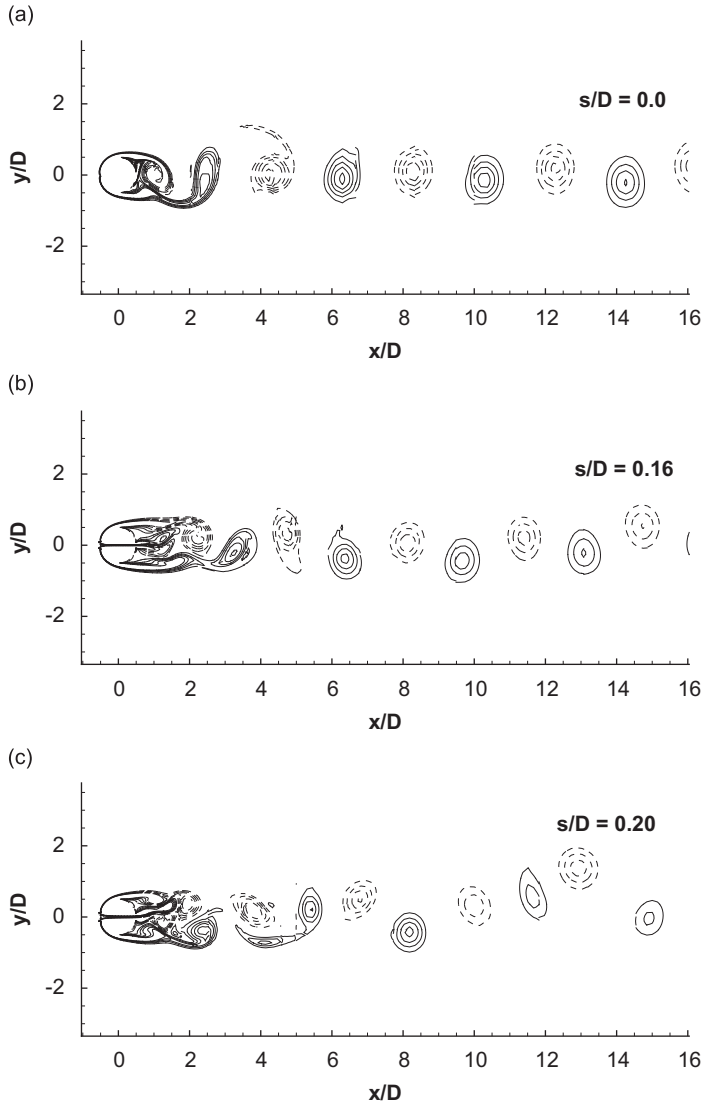

Fig. 2. Vorticity contour plots: (a) ST1, (b)ST5, (c) ST6.

number increases, and the *detuning process* of the slit jet starts at a smaller s/D ratio compared to the $\mathrm{Re} = 500$ cases. This behavior is very similar to the suction/blowing control reported in Dong et al. (2008).

We also confirmed the effectiveness of slit in 3-D flow at $\mathrm{Re} = 500$ with a cylinder that has the same cross-section as ST6. This simulation shows that the r.m.s. lift coefficient, C_L, is 0.0841, i.e., it is reduced by about 50% compared to $C_L = 0.174$ of the corresponding 2-D simulation (case ST6) as shown in Fig. 5. The transition from 2-D flow—uniform flow in spanwise direction—to 3-D takes place around non-dimensional time 200, almost immediately after the introduction of spanwise sinusoidal disturbances to the flow. From this simulation and from related work in Dong et al. (2008), we speculate that parallel slits suppress drag and lift forces more in 3-D flow than in 2-D flow simulations. However, further studies are required in order to obtain a definite conclusion about the effect of three-dimensionality on the VIV suppression.

The frequency spectrum of the lift force reveals that the superharmonics of the vortex shedding frequency disappear gradually as the slit ratio increases. It is noteworthy that up to $s/D = 0.12$, the dominant shedding frequency listed in Table 1 becomes smaller from $f = 0.2354$ to 0.2106. Case ST4 shows that frequency components drastically different from superharmonics observed in the reference cylinder start to grow as s/D increases. The spectrum of case ST5 shown

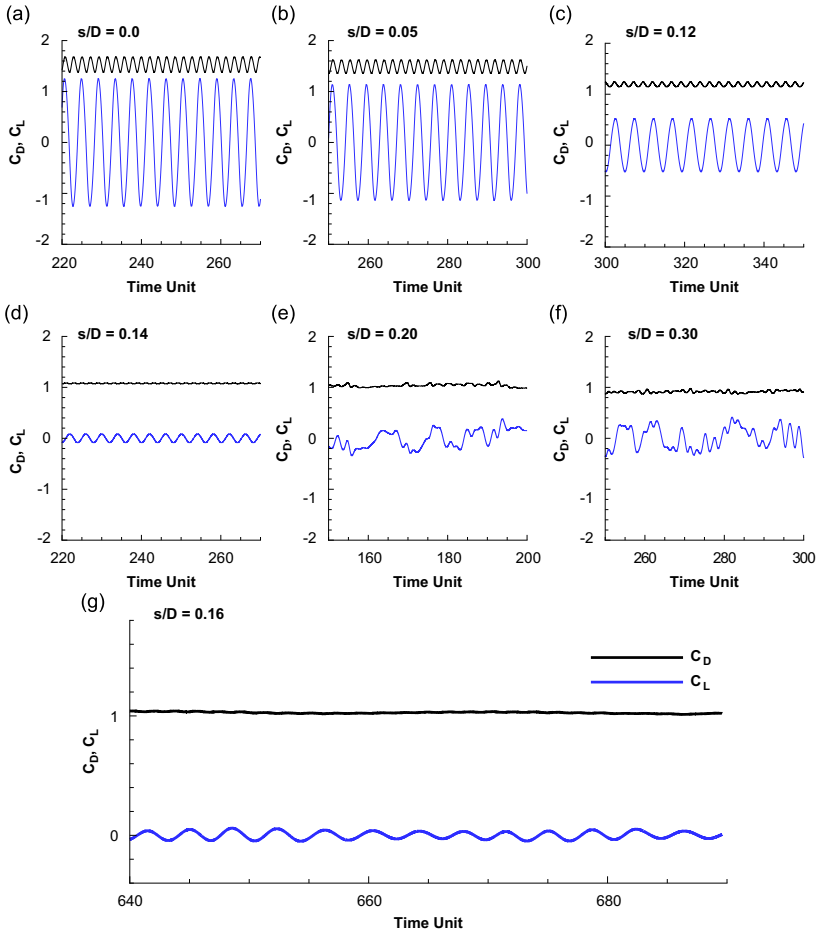

Fig. 3. Drag and lift force coefficients versus time: (a) ST1, (b) ST2, (c) ST3, (d) ST4, (e) ST6, (f) ST7, (g) ST5 at Re = 500.

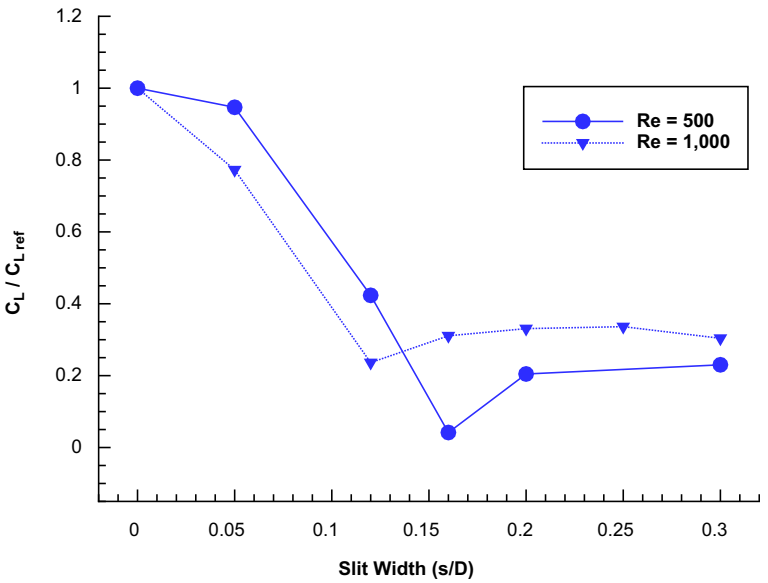

Fig. 4. R.m.s. lift coefficients versus normalized slit width at Re = 500 and 1000: lift coefficients are normalized with respect to C_L of the corresponding reference cylinder (ST1) for comparison purposes.

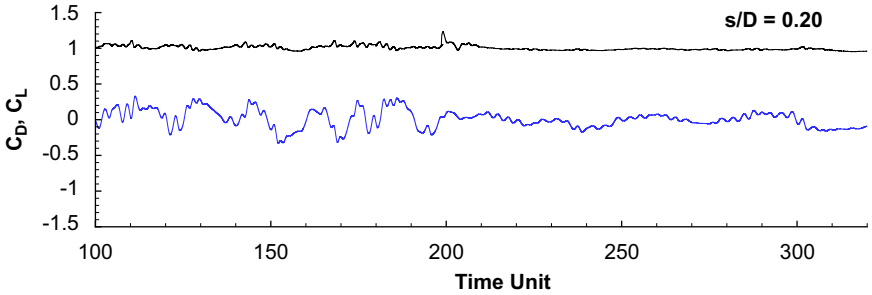

Fig. 5. 3-D simulation: drag and lift force coefficients per unit spanwise length versus time of a cylinder with slit ratio 20% at Re = 500. Spanwise sinusoidal disturbances for a short time interval are introduced to induce the transition of parallel vortex shedding to 3-D flow along the spanwise direction around time 200.

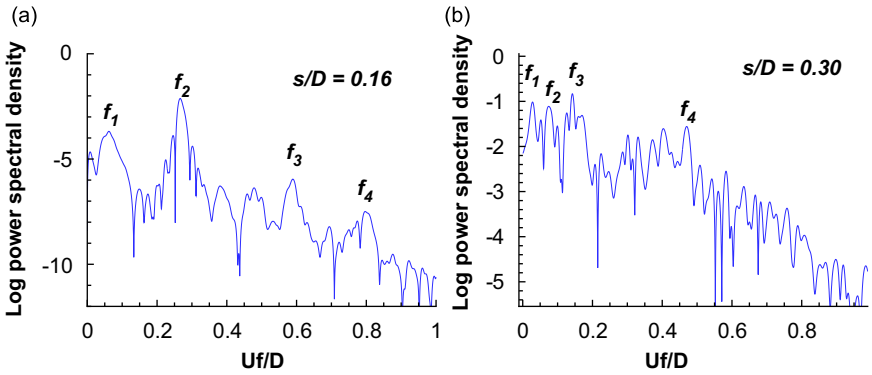

Fig. 6. Lift force power spectrum: (a) ST5, (b) ST7 at Re = 500.

in Fig. 6 loses most of superharmonics which are present in the reference cylinder case. In cases ST6 and ST7 those peaks disappear completely. This spectrum analysis confirms the *detuning process* caused by the slit more clearly.

The modified flow structure is intriguing and here we report on a very interesting transient vortex shedding pattern in case ST6, i.e., $s/D = 0.20$. In the beginning of simulation, vortex shedding from both the slit and outer walls of the cylinder are symmetric with shedding frequency 0.322−0.338 as shown in Fig. 7(a), which implies that the jet symmetric instability mode dominates. In contrast to the persistent 'antiphase' vortex shedding reported in Sumner et al. (1999) and Williamson (1985), the vortices shed from the slit decay within two diameters downstream from the cylinder while the ones from the outer wall of the cylinder are persistent with streamwise and transverse spacing of $1.9D$ and $1.27D$, respectively, at $x/D > 4.0$. The flow symmetry begins to break around $tU/D = 60.5$, when the simulation starts from quiescent flow condition, i.e., after shedding 20 pairs of symmetric vortices. From this time on, the vortices with opposite sign or same sign interact erratically and cancel each other or are strengthened. This interaction also changes the paths of shed vortices as shown in Fig. 7(c). Even during irregular vortex shedding, weak symmetric shedding was observed sporadically.

3.2. VIV: Y-motion

We also performed 2-D simulations of a rigid cylinder, which is allowed to move along the Y direction. For VIV simulations, three parameters are necessary to define the property of a cylinder: mass ratio, damping, and natural frequency. The non-dimensional natural frequency of a cylinder, $\omega_n = 2\pi \times 0.225$, is chosen to be close to the Strouhal number of a fixed cylinder at Re = 500. Since positive damping decreases the VIV of a cylinder, the damping coefficient was set to 0 or 0.01 to maximize the motion. The mass ratio is set to 3 which is close to the density ratio of risers used in the ocean. With these fixed parameters, several simulations with different slit ratios were performed and listed in Table 2. Simulations with larger mass were also performed, but here we present only the cases of mass ratio 3 since cylinders with the larger mass ratio show smaller amplitudes. In the cases VY1 and VY2, a positive structural damping

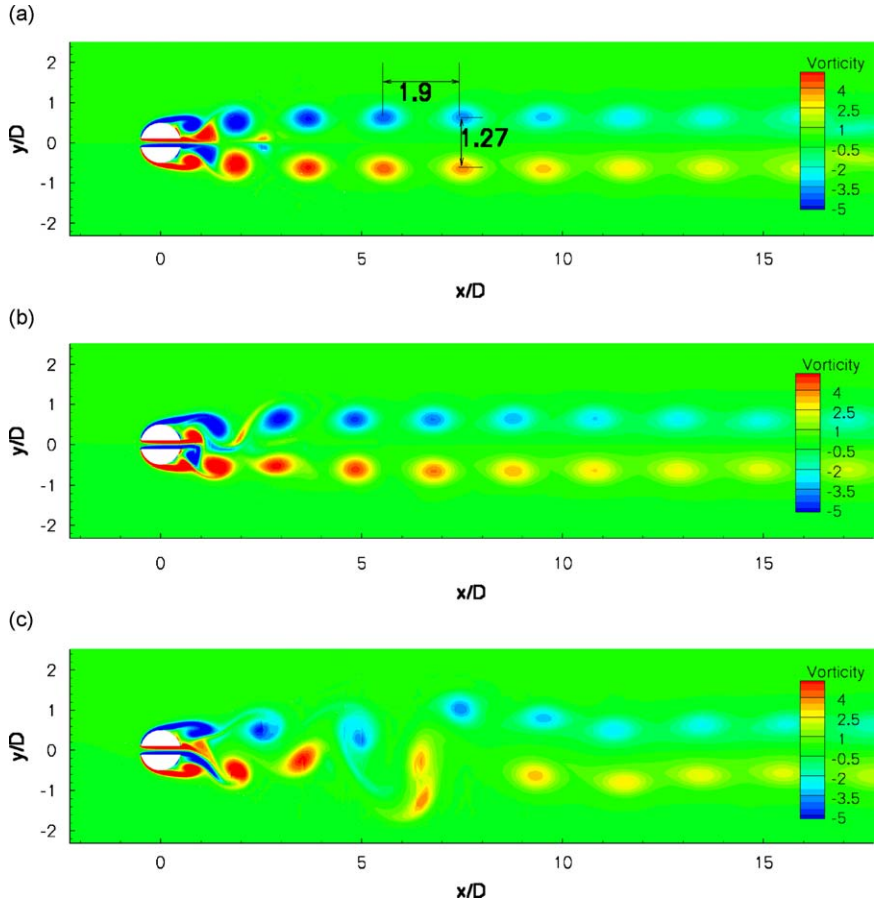

Fig. 7. Transition from symmetric to chaotic vortex shedding of case ST6 at $tU/D =$ (a) 55.5, (b) 60.5, and (c) 68 at $\mathrm{Re} = 500$. Initially the velocity field is set to zero; (b) shows the snapshot of vorticity distribution at the onset of the asymmetric shedding.

Table 2
Peaks at the power spectrum of Y displacement.

Cases	s/D	f_1	f_2	f_3	f_4
VY1	0.0	0.230(1.923)	0.461(−1.927)	0.692(−4.172)	0.923(−5.906)
VY2	0.12	0.218(1.176)	0.654(−5.035)	0.783(−6.643)	0.956(−8.215)
VY3	0.16	0.079(−3.056)	0.221(−2.5518)	0.257(−2.456)	0.474(−6.138)
VY4	0.20	0.077(−1.434)	0.202(−1.633)		
VY5	0.30	0.057(−1.708)	0.177(−1.02)	0.294(−2.492)	

In all cases, $\mathrm{Re} = 500$, damping 0.0, and mass ratio 3. Numbers in parentheses are magnitudes in log scale at the corresponding frequency.

coefficient causes reduction of the amplitude of the motion by about 10%. The Y-motion almost disappears in case VY3 as shown in Fig. 8.

The power spectrum of the cylinder transverse motion shown in Fig. 9 shows similar trends as the ones observed in the fixed cylinder cases. The strong energy around the superharmonics of shedding frequency spreads out to surrounding frequencies gradually as the slit ratio increases. Persistent dominant frequencies but reduced motion indicates that the suppressed motion is induced by the stretched vortex formation length. Detuning leads to shorter vortex formation length and larger motion in cases VY4 and VY5 than in the optimal case VY3.

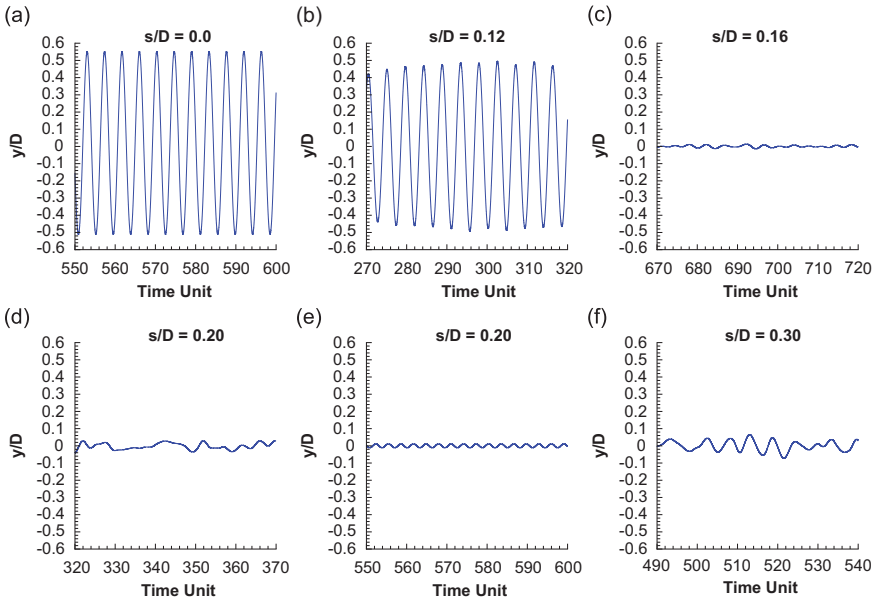

Fig. 8. Cylinder Y displacement: (a) VY1, (b) VY2, (c) VY3, (d) VY4, (e) VY4 with damping $= 0.01$, (f) VY5 at $V_r = 4.44$ and $\mathrm{Re} = 500$.

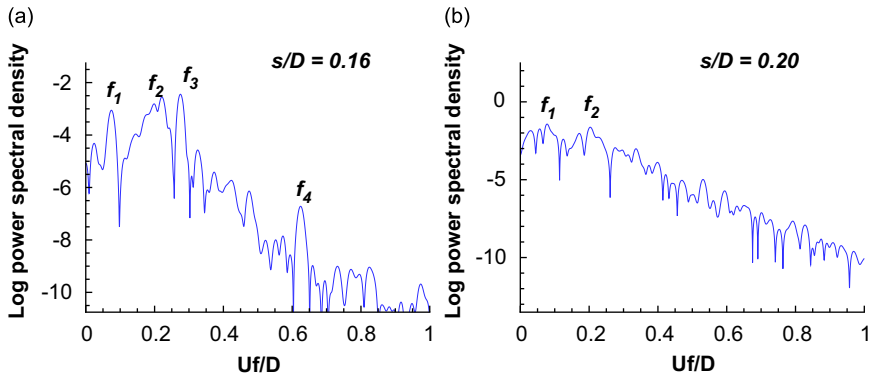

Fig. 9. Spectrum of Y displacement of (a) VY3 and (b) VY4.

For cases VY1 and VY3, we varied the reduced velocity, V_r, by changing the natural frequency of the system, $f_n = 0.225$ ($V_r = 4.44$) to 0.1, 0.14, 0.18, 0.20, 0.24, 0.27, 0.30, 0.33, 0.45, which correspond to $V_r = 10$, 7.14, 5.55, 5.0, 4.16, 3.70, 3.33, 3.03, 2.22. The Y displacements of 'control' cases, i.e., a cylinder with a slit of width 16% of the cylinder diameter, shows only 20% of the corresponding 'no control' cases around $V_r = 4$. The peak of control cases in Fig. 10 is much smaller in magnitude and narrower along the V_r-axis.

3.3. VIV: XY-motion

Guided by the results of the Y direction VIV simulations, we also performed VIV simulations of free cylinders. In the cases VXY1 and VXY2 listed in Table 3, a positive structural damping coefficient reduced the amplitude of the motion by about 10%. Fig. 11 shows that case VXY3 with $s/D = 0.16$ is still effective in suppressing the XY motion as well as Y motion, with the limit cycle of the cylinder being close to a fixed point. As observed in the cases of Y-motion simulations, spectrum analysis of the Y displacement reveals that detuning is starting from case VXY2 as shown in Fig. 12, and the vortex shedding superharmonics disappear in case VXY3 completely. Both Y-only and XY VIV

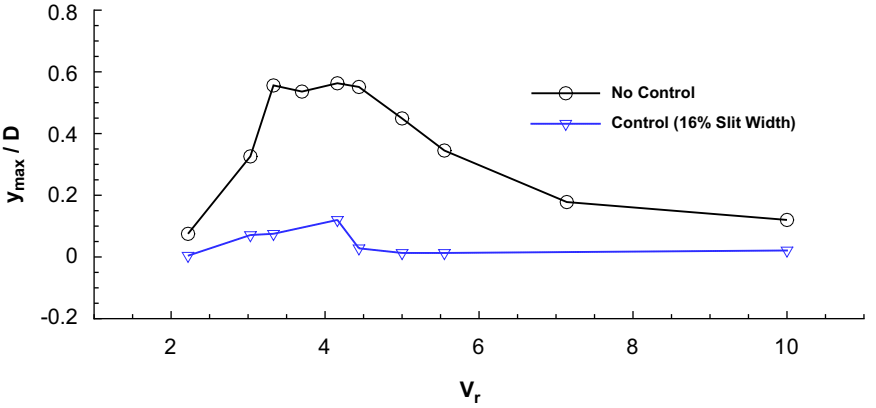

Fig. 10. Y displacement versus reduced velocity at Re = 500.

Table 3
Peaks at the spectrum of Y motion in XY VIV simulations.

Cases	s/D	f_1	f_2	f_3	f_4
VXY1	0.0	0.230(1.953)	0.462(−3.152)	0.693(−4.172)	0.921(−5.906)
VXY2	0.12	0.216(1.176)	0.363(−5.035)	0.652(−6.643)	0.797(−8.215)
VXY3	0.16	0.216(−2.123)	0.276(−2.677)	0.584(−7.81)	0.76(−8.933)
VXY4	0.20	0.065(−1.503)	0.323(−2.359)		
VXY5	0.30	0.174(−1.299)	0.323(−2.719)	0.488(−4.416)	

In all cases, Re = 500, damping 0.0, and mass ratio 3. Numbers in parentheses are magnitudes in log scale at the corresponding frequency.

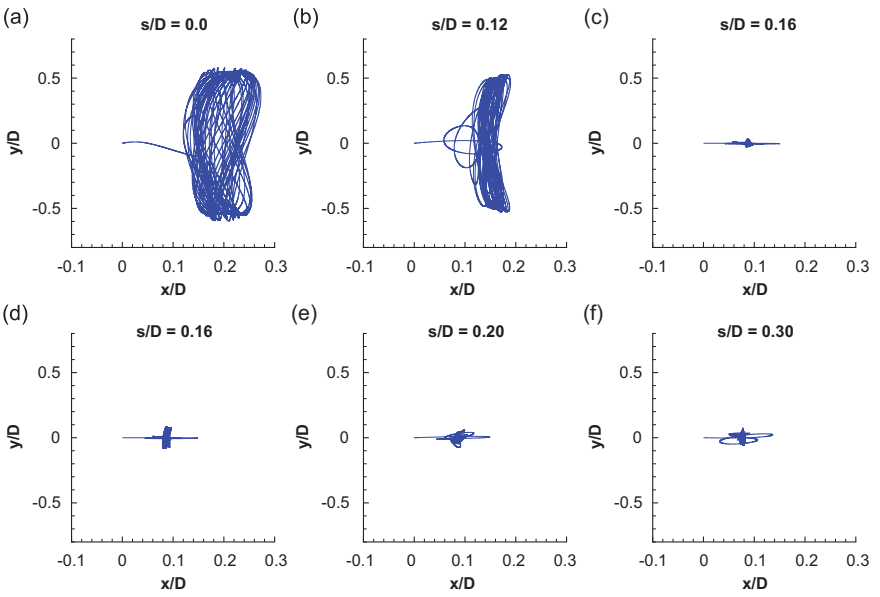

Fig. 11. Cylinder planar displacement trajectories: (a) VXY1, (b) VXY2, (c) VXY3, (d) VXY3 with damping = 0.01, (e) VXY4, (f) VXY5 at $V_r = 4.44$ and Re = 500.

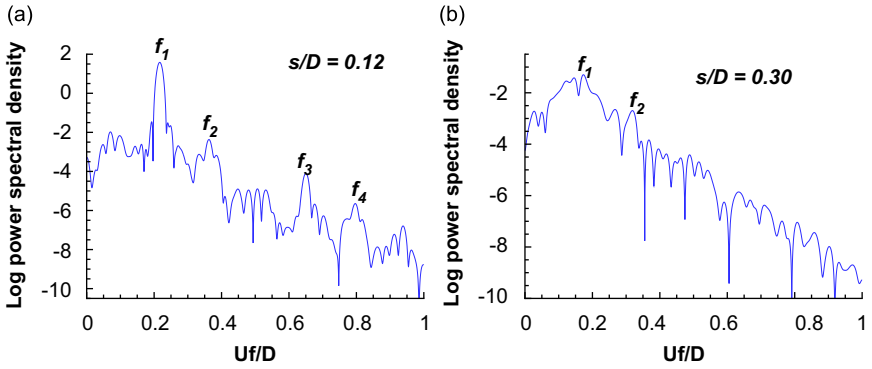

Fig. 12. Spectrum of Y motions of case (a) VXY2 and (b)VXY5.

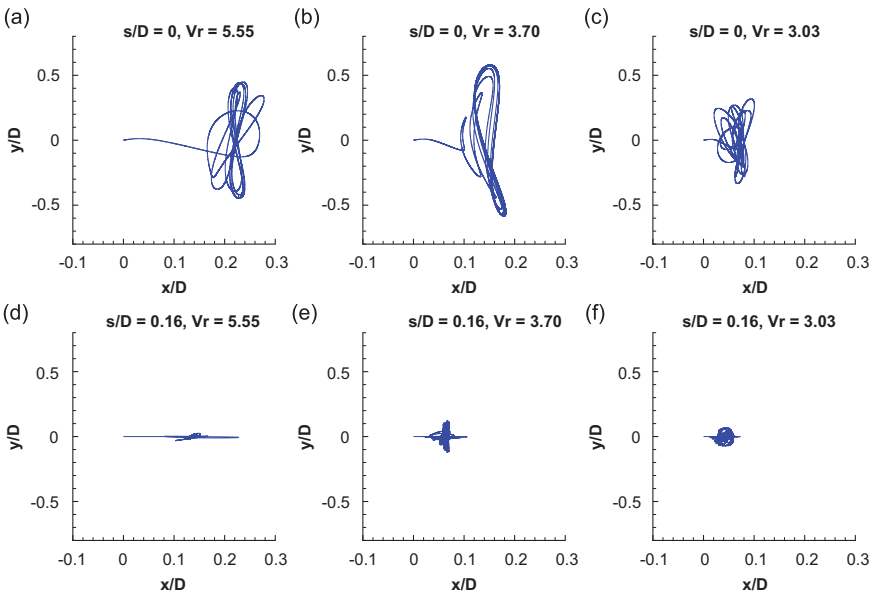

Fig. 13. Cylinder planar displacement trajectories of 'no control' cases (top row) and corresponding 'control' cases (bottom row) at Re = 500. V_r = (a, d) 5.55, (b, e) 3.70, (c, f) 3.03.

simulations start from the fully developed flow with the cylinders fixed at the origin. Subsequently, cylinders were released to move along either the Y-only or the XY direction(s).

As we tested crossflow (Y) VIV in a wide range of the reduced velocity, the same frequencies, $f_n = 0.1$, 0.14, 0.18, 0.20, 0.24, 0.27, 0.30, 0.33, 0.45, were adopted for VIV simulations of totally free cylinders with the same cross-section of cases VXY1 and VXY3. Maximum displacements in Y direction versus the reduced velocity show very similar patterns as observed in the crossflow-only VIV. The peak reduces dramatically by 75% in magnitude and the width of the peak is narrow. The Y displacements become almost negligible above $V_r = 4.5$ in XY VIV as well as in Y VIV. XY motion trajectories of representative cases with $V_r = 3.03$, 3.70, 5.55 are shown and contrasted between 'control' and 'no control' cases in Fig. 13; they clearly demonstrate the effective control of XY VIV via a slit.

4. Linear stability analysis

We carried out stability analysis of the wake flow using a local linear stability theory (Triantafyllou et al., 1986). During the stationary cylinder simulations, temporal averages of flow fields were obtained and the streamwise velocity

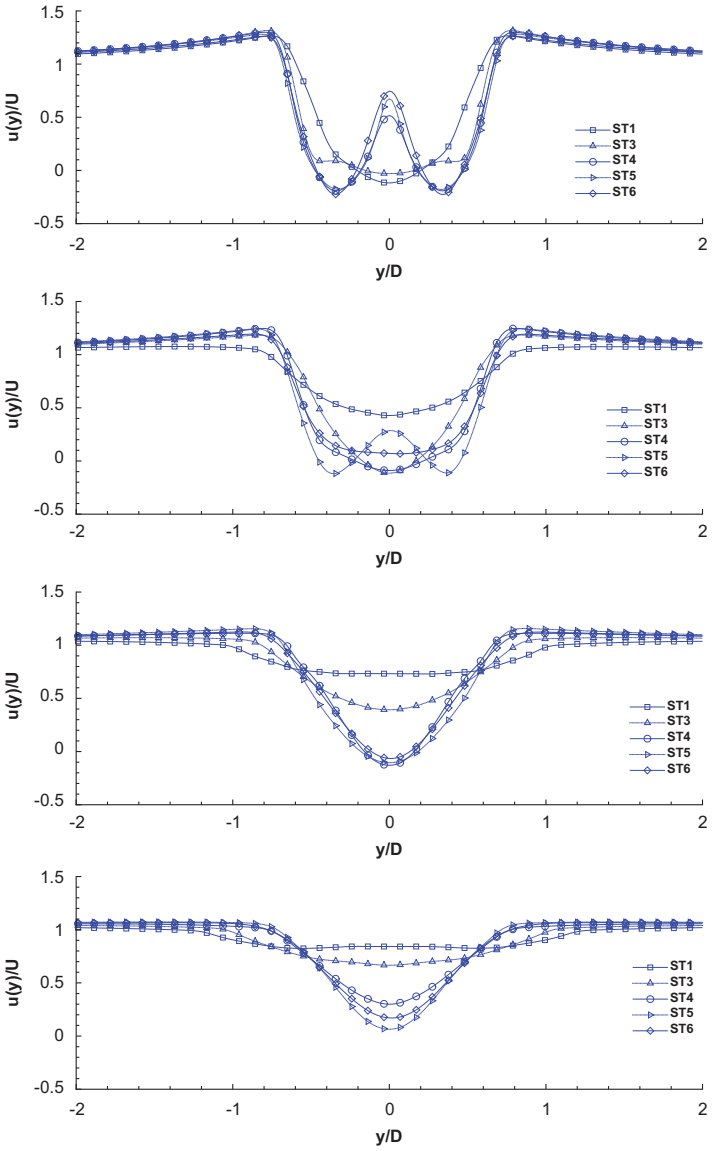

Fig. 14. $u(y)$ profile of the time-averaged flow: from top to bottom, $x/D = 0.8, 1.4, 2.0, 2.6$ at $\mathrm{Re} = 500$.

profiles at different x stations in the wake were extracted, see Fig. 14. These velocity profiles were used as base profiles for the stability analysis under the assumption that the streamwise velocity profile in a wake does not change significantly along the streamwise direction. It is interesting to note that cases ST1 and ST3 recover 80% and 50% of the incoming flow velocity at $x/D = 2.0$ while the other cases ST4, ST5, ST6 do not. In particular, case ST5 shows the highest momentum deficiency even at $x/D = 2.6$ and the velocity recovery is slower than case ST6 with larger slit ratio.

The inviscid Orr–Sommerfeld equation is solved numerically to find the dispersion relation $\omega = \omega(k)$ which maps k_i constant lines onto the ω-plane at each x stations as in Triantafyllou et al. (1986). From the similarity in the shape of the quadratic mapping, we identify the double root with the sign of the imaginary part determining whether the flow is convectively or absolutely unstable. If the double root (which looks like a cusp on the ω-plane) is above the ω_r-axis, the instability is absolute; if it is below the ω_r-axis, it is convective.

Streamlines in the averaged flow fields show a very interesting change of the fields as the slit width increases. These changes are directly reflected in the linear stability analysis. Fig. 15 shows the location of vortex systems in the time-

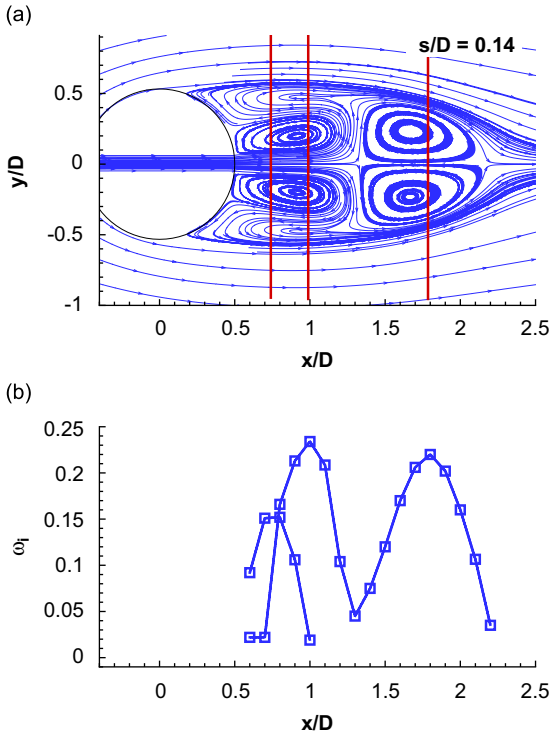

Fig. 15. (a) Streamlines in the time-averaged flow of ST4 with vertical lines indicating the location of the local maximum growth rate. (b) Peak growth rate (ω_i) versus x/D.

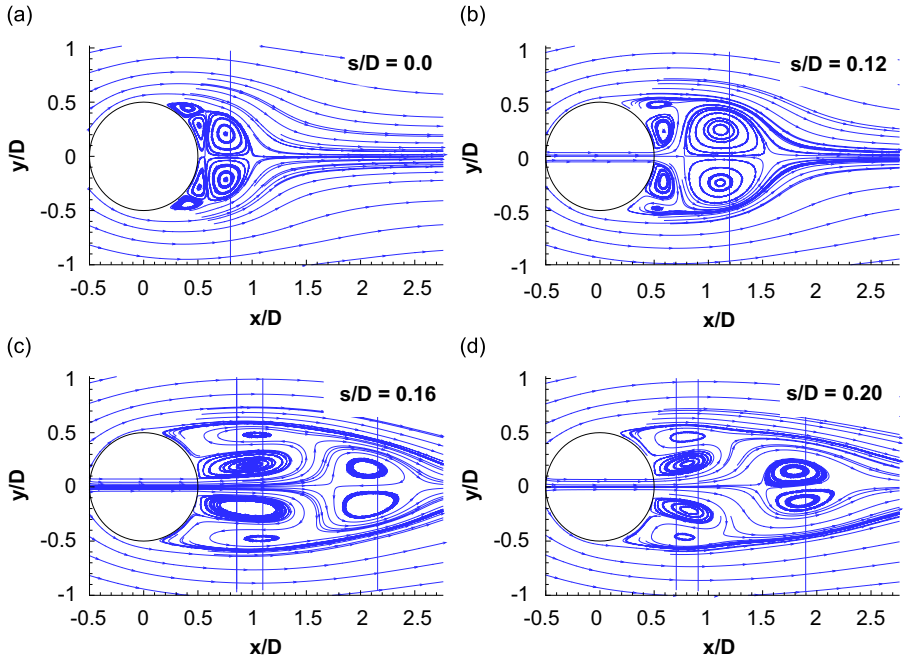

Fig. 16. Streamlines drawn from average velocity field: (a) ST1, (b) ST3, (c) ST5, (d) ST6. The vertical lines indicate the location where the linear stability analysis predicts the strongest local absolute instability.

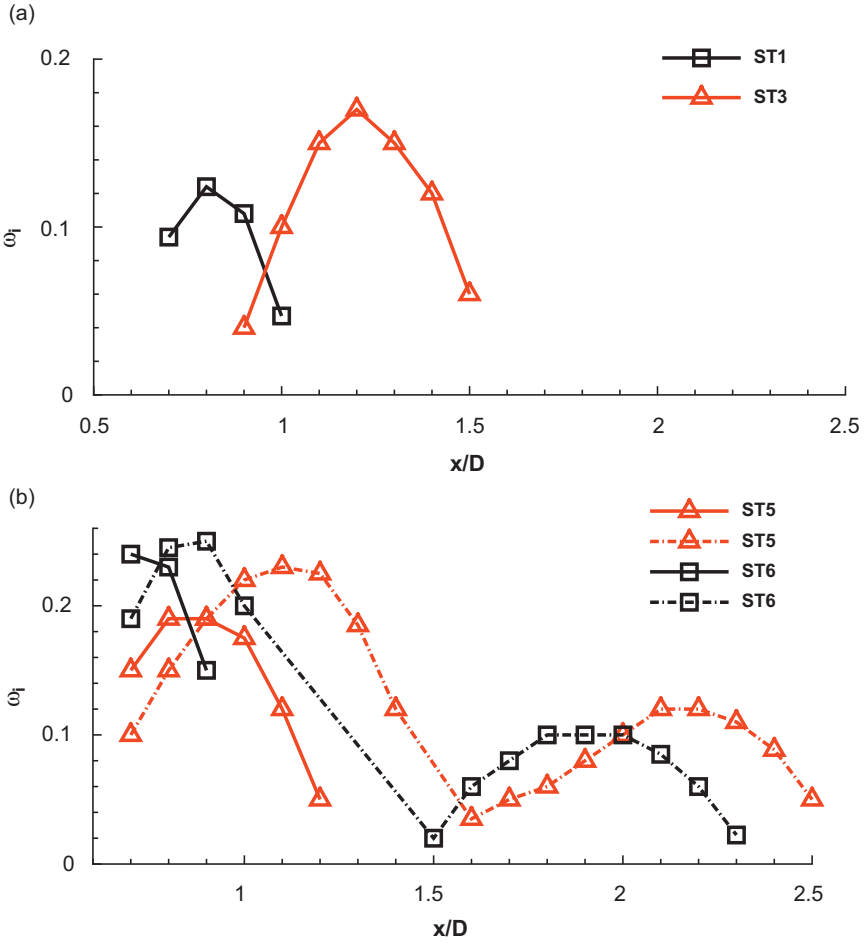

Fig. 17. Peak growth rate (ω_i) versus x/D: (a) ST1, ST3, (b) ST5, ST6.

averaged field of case ST4 and the positive growth rate of disturbances along the x/D stations. We check this relation for other cases as shown in Fig. 16. It is obvious that the recirculating zones near the base of the cylinder expand as the slit ratio increases. We want to point out that a secondary vortex system develops at $\mathrm{Re} = 500$ with the secondary vortices attached to the cylinder wall; this is not present in the average flow field at $\mathrm{Re} = 100$. The vortex systems are shifted downward farthest in case ST5, creating saddle points at $x/D = 1.7$ and 2.4. Vertical lines shown in Fig. 16 are drawn at the locations of local maxima of disturbance growth rate predicted with the stability analysis. Their locations are close to the centers of the vortices with a small offset.

For linear local stability analysis, base velocity profiles, i.e., u velocity profiles, were extracted at $x/D = 0.7, 0.8, \ldots, 2.6$ from the averaged flow field. The stability analysis with the reference cylinder was performed as a benchmark test predicting a Strouhal number, 0.2476, which differs from the vortex shedding frequency, 0.2345 by 5.2%. The growth rates of absolute instability are shown in Fig. 17. As the slit width increases, the temporal wave numbers at the double roots could not be directly related to the Strouhal number.

For cases ST4, ST5, and ST6, the map of constant k_i lines have two pinch points (double root of $\omega(k) = 0$) and this seems to be related to the vortex system induced by the jet flow through the slit. Case ST3 shows that the absolute instability zone is shifted downward even though the max growth rate is larger than that of case ST1. In cases ST5 and ST6, two absolute instability pockets shown as humps in Fig. 17 are getting closer to the cylinder while they are separated by a band of convective instability that covers $1.4 < x/D < 1.6$ and $1.1 < x/D < 1.4$, respectively. As s/D increases, this band gets wider along the streamwise direction.

Table 4
Shelled cylinders simulation configurations: R_i and R_o are the radius of the inner cylinder and the outer shell, respectively.

Cases	R_i	R_o	Description
TE1	0.5	0.55	Opening width 0.24 and two outlets
TE2	0.5	0.55	Opening width 0.6 and two outlets 0.24
TE3	0.25	0.5	Opening width 0.4
TE4	0.4	0.5	Opening width 0.4
TE5	0.5	0.75	Opening width 0.36
TE6	0.5	0.75	Rotate TE5 by 25°
TE7	0.125	0.5	Opening width 0.4
TE8	0.125	0.5	Inlet, outlet opening width 0.45, 0.25, respectively

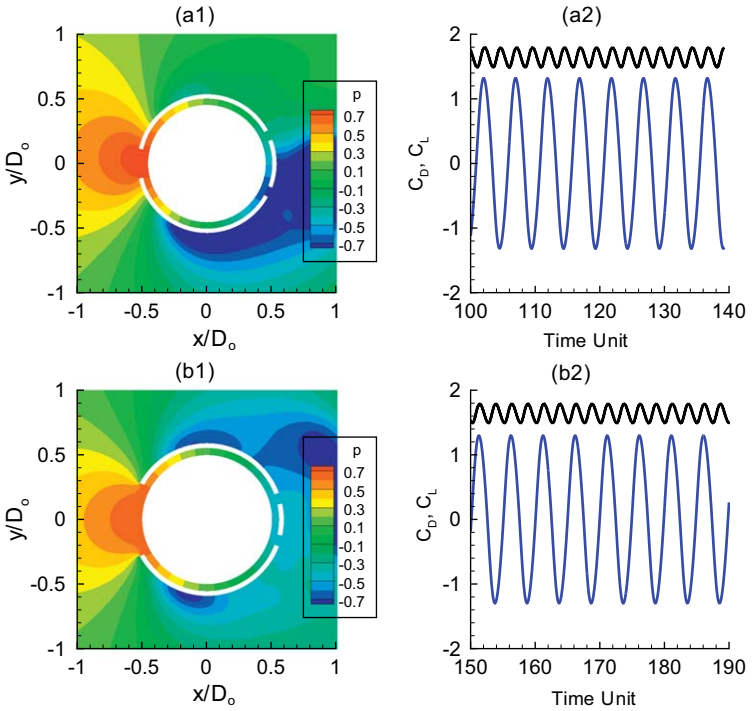

Fig. 18. Shell configurations showing instantaneous pressure distribution and corresponding time history of drag/lift force (total force on the shell and the cylinder) coefficient: (a) TE1, (b) TE2.

5. Alternative geometry modification

Cylinders partially covered with thin shells were investigated as an alternative design for suppressing VIV and potentially as a practical implementation of jet flow through slits. Table 4 shows some configurations with different R_i and R_o, which are the radii of the inner cylinder and outer shell, respectively. The thickness of the shell does not vary but is fixed at 0.04. Various configurations are possible but we mainly focused on one inlet and one or two outlet dents with varying outlet angles. Figs. 18–21 show the main configurations studied and their corresponding lift and drag force time histories. Lift and drag forces are sums of forces on the shell and the cylinder.

Cases TE1 and TE2 show a close similarity to the reference cylinder without a shell. Comparison of cases TE1 and TE2 with other cases indicates that the clearance between the shell and the inner cylinder is too small to create a strong jet into the near wake at $\mathrm{Re} = 500$. When the jets at the outlets are weak, separating outlets into two and positioning

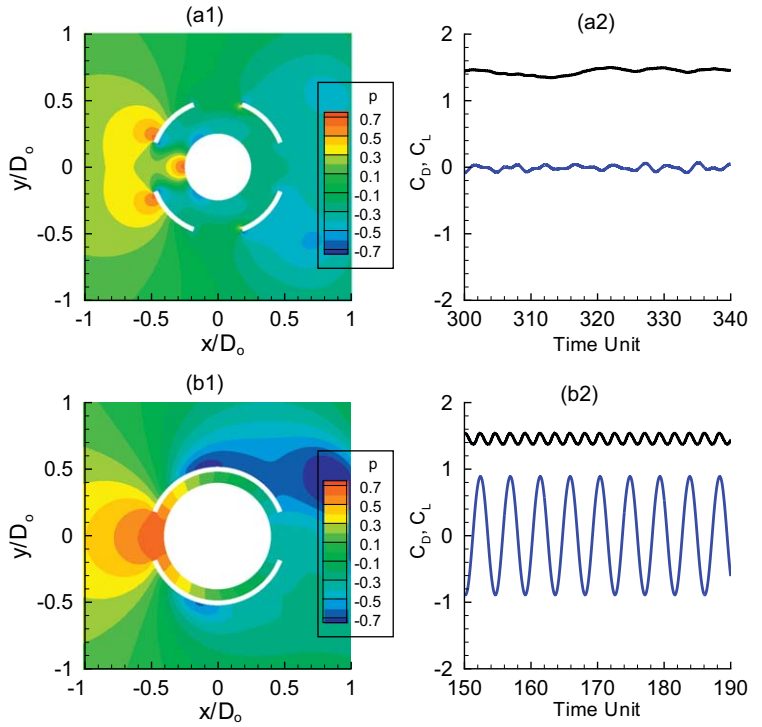

Fig. 19. Shell configurations showing instantaneous pressure distribution and corresponding time history of drag/lift force (total force on the shell and the cylinder) coefficient: (a) TE3, (b) TE4.

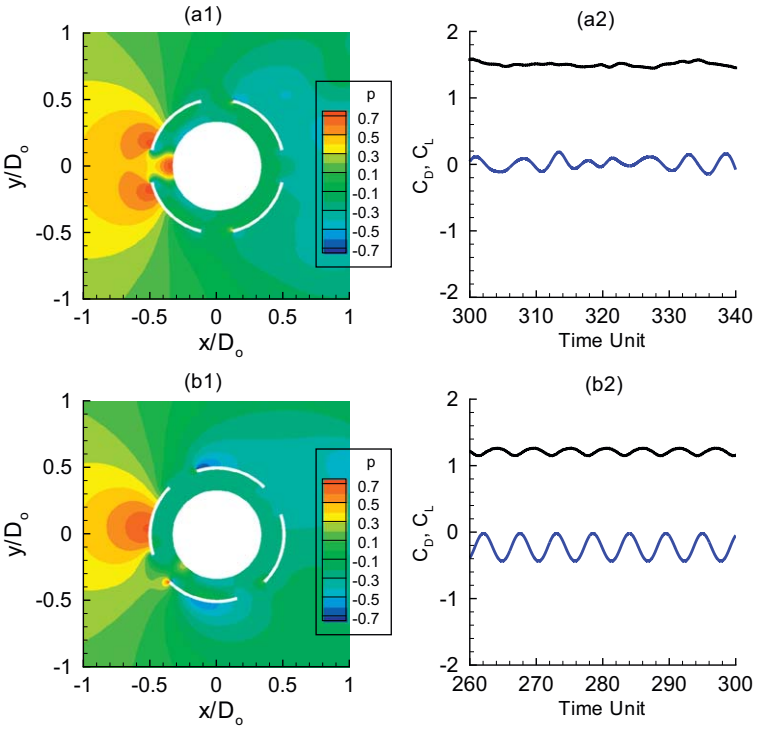

Fig. 20. Shell configurations showing instantaneous pressure distribution and corresponding time history of drag/lift force (total force on the shell and the cylinder) coefficient: (a) TE5, (b) TE6.

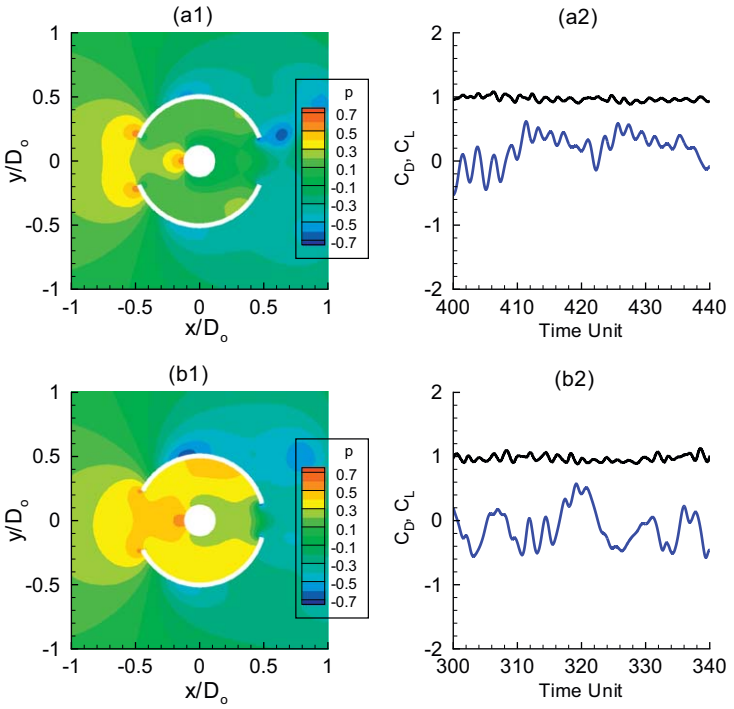

Fig. 21. Shell configurations showing instantaneous pressure distribution and corresponding time history of drag/lift force (total force on the shell and the cylinder) coefficient: (a) TE7, (b) TE8.

them at different angles does not seem to affect the lift. However, it is anticipated that TE1 and TE2 configurations work better either when the clearance gets larger or when the Reynolds number increases, as we observed that the optimal slit width gets smaller when the Reynolds number increased from 500 to 1000. In cases TE3 and TE4 whose outer shell radii are equal to that of the reference cylinder, the drag forces change slightly. The lift force, however, can be almost negligible if the inner cylinder has the right size as case TE3 shows. A too small inner cylinder, however, does not reduce the lift force since the interaction between the wake flows from the inner cylinder and the outer shell is not beneficial to the reduction in lift forces, as we found in cases ST6 or cases TE7 and TE8. Hence, as we saw in the slit cases, we expect the existence of an optimal ratio of the radius of cylinder to that of the outer shell. Case TE5 shows drastic lift force suppression while the drag force increases almost twice compared to the reference cylinder of radius 0.5, because of the increased cross-sectional area introduced by the outer shell. Case TE6 has the same geometry but the outer shell is rotated around the center of the cylinder by 25° from the case TE5. This case shows that the lift force is still suppressed with a slight downward bias; the drag force is also reduced by 30%. Cases TE7 and TE8 show the best performance in terms of drag force reduction which can be explained from the small cross-sectional area of the inner cylinders and shells. However, the lift forces can be as high as 60−70% of the uncontrolled reference case.

6. Conclusions

We have investigated the hydrodynamic effect of small slits on the wake flow and VIV through 2-D and 3-D simulations of flow past a circular but modified cylinder. A slit is placed parallel to the incoming flow along the diameter of a circular cylinder, and its slit width was varied from 0% to 30% of the diameter of the cylinder. The effect of slits was tested for both fixed and free cylinders using simulations based on the high-order spectral/hp element method. A series of systematic runs demonstrated that a slit parallel to the incoming flow is a very effective way to suppress the lift and VIV by modifying the wake flow. Over a wide range of the reduced velocity, a parallel slit maintains impressive performance of more than 70% reduction of Y displacement both in the Y-only VIV and XY VIV.

Modified cylinders with a slit of sufficiently large width produce a strong jet flow into the wake that changes the vortex shedding pattern dramatically. For slits of larger than optimal width—16% and 12% at $Re = 500$ and 1000, respectively—visualizations of the instantaneous flow fields do not show periodic vortex shedding patterns. The existence of optimal slit width at $Re = 500$ and 1000 shows that the reduced drag and lift are ascribed not to the reduced frontal area but to the change of instability regions and their interactions. A 3-D simulation of a stationary cylinder with slit ratio 20% at $Re = 500$ showed 50% reduction of r.m.s. lift force compared to the corresponding 2-D simulation.

Plots of the averaged flow showed that slits strengthen the secondary vortex system attached to the cylinder. A local linear stability analysis was carried out using the averaged flow to find the changes in the size and location of the absolute instability zones. Slits do not completely change the instability mode from absolute to convective even though Dong et al. (2008) reported that suction/blowing method does. A closer implementation of the suction/blowing idea of Dong et al. (2008) could be possibly pursued using a series of microchannels creating a porous wall and possibly directing the flow at certain angles in the rear of the cylinder. Another open issue is the use of discontinuous slits along the span, which according to Dong et al. (2008) seems to be more effective in suppressing VIV. Also shelled cylinders in the same spirit of creating jet flows into the near-wake were tested; configurations with appropriate gap and dent size showed very promising results with suppressed drag and lift coefficients.

Finally, we note that, after we completed our simulation studies, we became aware of some industrial (PETROBRAS) experimental work presented in Fernandes et al. (2008) that has tested ideas similar to ours at higher Reynolds number (10 000–40 000). This experimental study demonstrates independently that strong jets into the near wake are effective in VIV suppression.

Acknowledgments

This research was supported by ONR (Thomas Swean). The simulations were performed on the IA-64 TeraGrid Linux Cluster systems at NCSA and SDSC.

References

Bearman, P.W., 1973. The interaction between a pair of circular cylinders normal to a stream. Journal of Fluid Mechanics 61, 499–511.

Dong, S., Triantafyllou, G.S., Karniadakis, G.E., 2008. Elimination of vortex streets in bluff-body flows. Physical Review Letters 100, 204501.

Evangelinos, C., Karniadakis, G.E., 1999. Dynamics and flow structures in the turbulent wake of rigid and flexible cylinders subject to vortex-induced vibrations. Journal of Fluid Mechanics 400, 91–124.

Fernandes, A.C., Coelho, F.M., Franciss, R., 2008. VIV control and drag reduction using the guided porosity concept. In: OMAE2008-57471, Proceedings of the 27th International Conference on Offshore Mechanics and Arctic Engineering, Estoril, Portugal, June 15–20.

Igarashi, T., 1978. Flow characteristics and a circular cylinder with a slit. 1st report, flow control and flow patterns. Bulletin of JSME 21, 656–664.

Karniadakis, G.E., 1990. Spectral element-Fourier methods for incompressible turbulent flows. Computer Methods in Applied Mechanics and Engineering 80, 367–380.

Karniadakis, G.E., Sherwin, S.J., 2005. Spectral/hp Element Methods for CFD. Oxford University Press, Oxford.

Karniadakis, G.E., Triantafyllou, G.S., 1989. Frequency selection and asymptotic states in laminar wakes. Journal of Fluid Mechanics 199, 441–469.

Kim, H.J., Durbin, P.A., 1988. Investigation of the flow between a pair of circular cylinders in the flopping regime. Journal of Fluid Mechanics 196, 431–448.

Kim, J., Choi, H., 2005. Distributed forcing of flow over a circular cylinder. Physics of Fluids 17, 1–16.

Lee, K., Yang, K.-S., Yoon, D.-H., 2009. Flow-induced forces on two circular cylinders in proximity. Computers and Fluids 38, 111–120.

Lin, J., Towfighi, J., Rockwell, D., 1995. Near-wake of a circular cylinder: control by steady and unsteady surface injection. Journal of Fluids and Structures 9, 659–669.

Naudascher, E., Rockwell, D., 1994. Flow-induced Vibrations: An Engineering Guide. A.A. Balkema, Rotterdam.

Newman, D., Karniadakis, G.E., 1997. A direct numerical simulation study of flow past a freely vibrating cable. Journal of Fluid Mechanics 344, 95–136.

Olsen, J., Rajagopalan, S., 2000. Near-wake of a circular cylinder: control by steady and unsteady surface injection. Journal of Wind Engineering and Industrial Aerodynamics 86, 55–63.

Persillon, H., Braza, M., 1998. Physical analysis of the transition to turbulence in the wake of a circular cylinder by three-dimensional Navier–Stokes simulation. Journal of Fluid Mechanics 365, 23–88.

Sumner, D., Wong, S.S.T., Price, S.J., Päidoussis, M.P., 1999. Fluid behaviour of side-by-side circular cylinders in steady cross-flow. Journal of Fluids and Structures 13, 309–338.

Triantafyllou, G., Triantafyllou, M., Chryssostomidis, C., 1986. On the formation of vortex streets behind stationary cylinders. Journal of Fluid Mechanics 170, 461–477.

Williamson, C.H.K., 1985. Evolution of a single wake behind a pair of bluff bodies. Journal of Fluid Mechanics 159, 1–18.

Wood, C., 1964. The effect of base bleed on a periodic wake. Journal of the Royal Aeronautical Society 68, 447–482.